Materials Research Express

Electrical transport across nanometric $SrTiO_3$ and $BaTiO_3$ barriers in conducting / insulator / conducting junctions

To cite this article before publication: henry Luciano navarro *et al* 2017 *Mater. Res. Express* in press https://doi.org/10.1088/2053-1591/aaa2e7

Electrical transport across nanometric $SrTiO_3$ and $BaTiO_3$ barriers in conducting / insulator / conducting junctions

H. Navarro,[1,2] M. Sirena,[1,2] J. González Sutter,[1,2] H.E.Troiani,[2] P. G. del Corro,[1,2] P. Granell,[4] F. Golmar,[5] N. Haberkorn.[1,2]

[1] *Comisión Nacional de Energía Atómica and Consejo Nacional de Investigaciones Científicas y Técnicas, Centro Atómico Bariloche, Av. Bustillo 9500, 8400 San Carlos de Bariloche, Argentina.*

[2] *Instituto Balseiro, Universidad Nacional de Cuyo and Comisión Nacional de Energía Atómica, Av. Bustillo 9500, 8400 San Carlos de Bariloche, Argentina.*

[4] *INTI, CMNB, Av. Gral Paz 5445 (B1650KNA), San Martín, Buenos Aires, Argentina*

5 Consejo Nacional de Investigaciones Científicas y Técnicas, Escuela de Ciencia y Tecnología, UNSAM, Campus Miguelete, (1650), San Martín, Buenos Aires, Argentina.

Abstract: We report the electrical transport properties of conducting / insulator / conducting heterostructures by studying current – voltage IV curves at room temperature. The measurements were obtained on tunnel junctions with different areas (900 μm^2, 400 μm^2 and 100μm^2) using a conducting atomic force microscope. Trilayers with $GdBa_2Cu_3O_7$ (GBCO) as the bottom electrode, $SrTiO_3$ or $BaTiO_3$ (thicknesses between 1.6 nm and 4 nm) as the insulator barrier, and GBCO or Nb as the top electrode were grown by DC sputtering on (100) $SrTiO_3$ substrates For $SrTiO_3$ and $BaTiO_3$ barriers, asymmetric IV curves at positive and negative polarization can be obtained using electrodes with different work function. In addition, hysteretic IV curves are obtained for $BaTiO_3$ barriers, which can be ascribed to a combined effect of the FE reversal switching polarization and an oxygen vacancy migration. For GBCO/ $BaTiO_3$/ GBCO heterostructures, the IV curves correspond to that expected for asymmetric interfaces, which indicates that the disorder affects differently the properties at the bottom and top interfaces. Our results show the role of the interface disorder on the electrical transport of conducting/ insulator/ conduction heterostructures, which is relevant for different applications, going from resistive switching memories (at room temperature) to Josephson junctions (at low temperatures).

Keywords: Thin films; sputtering; conductive atomic force microscopy; tunnel junctions.

* *e-mail* corresponding author: henrynavarro@cab.cnea.gov.ar. Tel: +54 0294 444 5171- FAX: +54 0294 444 5299

1. Introduction

Conventionally, a tunnel junction (TJ) consists of two conducting electrodes and a nanometer-thick insulating barrier layer between them. The transmittance of a TJ depends exponentially on the height and the width of the barrier [1]. In solid state electronics, electron tunneling is exploited in the operation of devices such as magnetic random access memories (MRAM) [2], resonant tunneling diodes [3] and Josephson junctions for superconducting electrodes [4]. In addition, if a ferroelectric (FE) tunnel barrier is used, the device is called a ferroelectric tunnel junction (FETJs)[5]. In FETJs the tunnel transmission may be strongly modulated by switching the ferroelectric polarization, which modifies the potential barrier height and width [6]. For oxide based heterostructures, in addition to tunneling across the insulator barrier, other mechanisms such as oxygen vacancy migration (OVM) may contribute to the electrical transport [7]. OVM could produce forming/ deforming oxygen vacancy filaments [8,9] and Schottky barrier variations [10].The different contributions and mechanism are also affected by interfacial disorder (chemical inhomogeneity, strain and charge conservation), which can lead to a considerable deviation of the electrodes and barrier properties from those observed in bulk [11,12].

The tunneling transmittance across a barrier depends on the properties of the barrier and the electrodes [13]. The TJ are defined as "symmetric" or "asymmetric" depending on what electrodes are used (with similar or different work function (W)) [14]. Considering different disorder mechanisms, the effective barrier thickness can be either reduced by conducting interfaces [15] or increased by the presence of dead layers in the metallic electrodes [16]. For epitaxial perovskite heterostructures, $Ba_{1-x}Sr_xTiO_3$ and $BiFeO_3$ (BFO) insulator barriers are usually used [17,18]. $SrTiO_3$ (STO) is a dielectric material [19] and FE can be induced by strain [20]. $BaTiO_3$ (BTO) and BFO are FE materials and their properties usually depend on dimension and stress. The critical thickness for FE in epitaxial BTO [21,22,23] and BFO [24] thin films is ≈ 2 nm.

In this work, we study the electrical transport across conductive/ insulator/ conductive heterostructures using STO and BTO thin barriers. Epitaxial STO and BTO layers with thicknesses of 1.6 nm, 2.4 nm, 3.2 nm and 4 nm were grown on 16 nm thick $GdBa_2Cu_3O_{7-d}$ (GBCO) bottom electrode. FE was previously observed in GBCO/ 4 nm thick BTO bilayers [25]. Two different top electrodes were used, 16 nm thick GBCO and 55 nm thick Nb. GBCO is a material chemically and structurally compatible with STO (a = 0.3905 nm) and BTO (a =

0.399 nm). For optimal oxygen doping, its crystalline structure is orthorhombic with lattice parameters a = 0.383 nm, b = 0.389 and c = 1.17 nm. GBCO can be used as a conducting electrode for the normal state and as a superconducting electrode at temperatures below 92 K. The Nb component was selected because its work function is different from the GBCO´s and displays superconductivity at low temperature (superconducting critical temperature T_c = 9.3 K). The electrical transport of the TJ was analyzed from current versus voltage (IV) curves at room temperature using a conductive atomic force microscope (CAFM) assuming tunneling as the main electrical transport mechanism. The results indicate that the characteristic IV curves for the different systems depends on the nature of both conducting electrode that injects current and the type of insulator barrier.

2. Experimental methods

The bottom 16 nm thick GBCO and the top GBCO electrodes were grown on (100) STO by DC sputtering using the condition previously described in Ref [26]. The total pressure at the chamber was 400 mTorr (90:10, Ar: O_2). Following, the insulator (STO / BTO) barrier was grown by RF sputtering using 25 W. The 55 nm thick Nb top electrode was grown after cooling down the GBCO / insulator bilayers to room temperature using pure 10 mTorr Argon and 50 W. Trilayers with insulator (STO and BTO) barrier thicknesses ($d_{\text{Insulator}}$) of 1.6 nm, 2.4 nm, 3.2 nm and 4 nm were grown by using identical deposition conditions [25]. The GBCO and Nb growth rates were 2.3 nm/ min and 55 nm/ min, respectively. The STO and BTO growth rate was 1 nm/ minute. Wherever used, the notations [G-I_d-T] indicate a GBCO bottom and top (T) electrodes (Nb and GBCO (G)), and I, the insulator barrier (S: STO, B: BTO) with thickness d (nm). TJ with different areas (900 μm^2, 400 μm^2, and 100 μm^2) were fabricated by optical lithography. Before fabricating the TJ, the GBCO/ insulator/ GBCO heterostructures were covered with a 50 nm thick Ag silver film. The TJs were constructed removing the top conducting electrode using Ar ion etching. GBCO and Nb top electrodes were used to design symmetric and asymmetric devices, respectively.

The epitaxial growth of the GBCO and insulator layers was verified by X–ray diffractometry (XRD) using a Panalytical Empyrean equipment. The surface roughness of the samples was analyzed from atomic force microscopy (AFM) images. The microstructure of a GBCO / STO (4 nm) / GBCO trilayer was analyzed by transmission electron microscopy (TEM) using a

CM200 UT microscope operated at 200kV. For TEM analysis, a thin lamella was prepared with a Gallium focused ion beam (FEI Helios Nanolab 650). CAFM measurements were performed in a Dimension 3100 Bruker microscope, using diamond doped conductive tips. The topographical images of the samples were obtained at different scales (1 μm and 10 μm). Current-voltage (IV) curves were obtained using the ramp mode by putting the tip over the top electrode (with a silver capping layer) [27]. The minimum detectable current in the CAFM used was 50 pA, and the maximum was 480 nA, under a bias voltage ranging from 0.01 to 12 V. The bottom electrodes of the junctions were contacted scratching the corner of the samples with a diamond tip in order to break the barrier and access the bottom electrode bellow. The electrical contact was improved by adding silver paste to the area. Samples are measured in the two-point geometry and the series resistances were evaluated in several samples (gold reference thin film and GBCO single films contacted in the same way as describes before). The total series resistance is around 10 kΩ, given mainly by the tip-sample contact.

3. Results and discussion

The crystalline structure of the [G-I_d-G] heterostructures was examined by XRD and was found to be single phase with (00*l*) orientation (not shown)[26]. The microstructure of a [G-S_4-G] sample was analyzed by TEM. A typical cross section TEM image is shown in Figure 1*a*. The barrier displays steps which are mainly originated by the roughness of the bottom GBCO electrode (typical steps of 1 unit cell ≈ 1.2 nm) and they induce a structural disorder such as stacking faults [28]. For [G-I_d-Nb] trilayers, the microstructure of the GBCO electrode and the barrier are expected to be similar to those observed in Fig. 1*a.* Considering that the Nb top layer is grown at room temperature, the microstructure is polycrystalline. The evolution of the surface topology by adding the successive layers was measured by AFM in a [G-S_4-G] trilayer. The bottom GBCO electrode displays smooth surfaces with a root mean square (RMS) roughness of about 0.3 nm [29]. The roughness is systematically increased at the insulator barrier (RMS = 1.6 nm) and at the top GBCO electrode (RMS = 2.4 nm). The increment in the roughness could be mainly attributed to the nucleation around topological defects such as steps.

Figures 2*a-d* show the current density (*J*) as function of V for TJ with 4 nm thick insulator barriers and different junction areas. The curves present the characteristic semi-log

dependences expected for tunneling in the Fowler-Nordheim regime (F-N) (with V >ϕ /e, where ϕ is the barrier height) [13]. Positive voltage branches correspond to electrons tunneling from the top to the bottom electrode, and vice versa for negative voltage branches. Two outstanding features are observed in the *J* (V) dependences: (I) hysteretic curves are obtained for increasing-decreasing voltages at both positive and negative voltages in [G-B_4-G] and [G-B_4-Nb]; and, (II) asymmetric curves for positive and negative polarization branches are observed for [G-I_d-Nb]. The hysteretic IV curves appear for samples with BTO barriers, indicating that the FE polarization might be playing a significant role in the conductance [14]. On the other hand, the different conductivity observed at positive and negative branches for [G-I_d-Nb] samples can be associated with the properties (i.e. W) of the electrode which injects the electrons [14]. As mentioned above, positive V branches correspond to electrons injected from the Nb to the GBCO, whereas negative V branches correspond to electrons injected from the GBCO to the Nb.

In order to analyze the influence of the barrier thickness on the resulting electrical transport, *J*(V) curves for TJ with different barrier thickness (1.6 nm, 2.4 nm, 3.2 nm and 4 nm) and different areas (10x10 μm^2, 20x20 μm^2 and 30x30 μm^2) were performed. It has been previously mentioned that, for very thin STO and BTO barriers (d< 3 nm), an increment of the conductivity at the borders of topological defects is observed [25,29]. Figures 3*a-b* show typical *J* (V) curves for [G-S_d-Nb] and [G-B_d-Nb]. As expected, as the barrier thickness is increased, the *J* (V) curves systematically shift to the right due to the increment in the resistance (R = V/I) of the junctions. It is notorious that for [G-B-Nb], hysteretic curves can be observed for barrier thickness as thin as 1.6 nm. This indicates that features that can be related to tunneling across a FE barrier are observed close to the lower thickness limit theoretically reported [21] for BTO layers covered by GBCO. In addition, independently from the barrier thickness, similar *J*(V) dependences are observed for TJ with different sizes. This indicates that the same mechanism governs the electrical transport (the quality of the barrier is homogenous in the involved area), which is in agreement with our previous study where surfaces clean of defects for GBCO/ STO bilayers on areas as large as 100x100 μm^2 were reported [29].

The presence of hysteresis in [G-B-G] and [G-B-Nb] (which is reproducible over many V cycles) will be discussed below. Hysteretic *J*(V) curves have been theoretically predicted [14] and experimentally observed for FETJ [30]. In addition, OVM may produce hysteretic

behavior in resistivity states of conducting/ insulator/ conducting devices with ultrathin STO and BTO barriers [7]. For FETJ, R usually switches at the coercive voltage (V_c) in which the polarization reversal at the FE barrier is electric-field-induced [14]. In single-domain FE films it is expected that the polarization reversal occurs simultaneously at a critical electric field ξ_c and its value depends on the thickness of the ferroelectric barrier ($V_c \approx \xi.d$) [31]. For symmetric FETJ (electrodes with similar W), resistive switching occurs at voltages $\pm V_c$, which is evidenced as a step-like increase in the resistance. In addition, the two branches of the hysteretic IV loop only touch each other at V = 0 (never cross), i.e. that after the full polarization of the barrier at high electric fields, the junction switches from a low resistance state to a higher one when the sense of the voltage (current) is inverted. For asymmetric TJ (electrodes with different W), the step-like resistance change depends on the difference in W for the bottom and the top electrodes. In this case, the two branches of the hysteretic IV curve cross each other at V = 0, i.e. that after the full polarization of the barrier the junctions stay at the same resistance state when switching the applied voltage. For asymmetric junctions the high or low resistance state is determined, mainly, by the direction of the ferroelectric polarization. This effect vanishes for tunnel junctions with equal electrodes due to the symmetry of the system. The theoretically predicted IV curves for symmetric and asymmetric FETJ are schematized in Fig. 4 [14]. Summarizing, the shape of the IV curves for tunneling across FE barriers is determined by the asymmetric electrostatic potential at insulator / electrode interfaces and the depolarizing field (V_c) [14].

The IV curves for [G-B_d-G] and [G-B_d-Nb] (see Figs. 1*b* and 1*c*) correspond to the expected behavior for tunneling in asymmetric TJ. For instance, after further polarization at positive and negative voltages (±3 V), *J* is smaller for the positive branch (R is larger) and larger for the negative branch (R is smaller). In addition, the branches of the IV loop cross each other at V = 0. Although asymmetric features are naturally expected for [G-B-Nb], the asymmetric behavior observed for [G-B-G] requires a different analysis. A remarkable difference between the experimental and theoretical predictions for the IV curves in [G-B-G] and [G-B-Nb] is the absence of a step-like change in the resistivity [14]. In addition, the hysteretic behavior in the *J* (V) curves remains at high polarization voltages (not saturated as expected for FE reversal switching). The absence of step-like changes in the IV curves may be related to a distribution of V_c as a consequence of thickness fluctuations of the BTO barrier in small areas (nanometric FE domains). The absence of saturation (hysteretic behavior) at high voltages indicates that

the height of the barrier is affected by other mechanisms such as OVM [7]. In addition, the asymmetric behavior observed in J (V) for [G-B_d-G] indicates that the properties at the top and bottom GBCO / BTO interfaces are different. Moreover, the strong reduction in the hysteresis observed for [G-B_d-Nb] in comparison with [G-B_d-G], suggests that OVM at the GBCO / BTO interfaces contributes significantly to the shape of the IV curves. Unlike GBCO / STO interfaces (with low mismatch), higher disorder is expected at the GBCO / BTO interfaces as consequence of the differences in the lattice parameter (GBCO: a = 0.384 nm; b = 0.389 nm; BTO: a = 0.399 nm). It is known that the properties of the GBCO are strongly affected by the oxygen stoichiometry so the reduction in the doping ($6.3 \leq \delta \leq 7$) usually decreases the T_c along with the difference in the lattice parameters a and b [32,33]. In fact, stress at GBCO/ BTO/ GBCO interfaces should induce a rhombohedric distortion for the BTO and a tetragonal distortion for the GBCO (reducing the oxygen content). Changes in the oxygen stoichiometry at the interfaces are in agreement with the T_c suppression observed in ref. [25,34]. In addition, oxygen mobility produced by electrical polarization ($\propto$ V) may affect the barrier height inducing dead or insulator interfaces [35]. Basically, the effective barrier thickness can be described by $\delta = d + \delta(V)$, where δ is an effective change (increment / decrement) in the size of the barrier (see schematic picture in Figure 5) due to different voltage dependent acting mechanisms and due to asymmetric properties at the top and the bottom electrode / barrier interface. For instance (considering for simplicity that only one of the interfaces is affected by the change in the oxygen concentration), OVM induced by the electrical field changes the oxygen stoichiometry at the interface and reduces the barrier width (leading to a low resistance state). Additionally, when the electrical polarization, i.e. applied voltage, is reduced the barrier width doesn't change (the low resistance state remains) until the voltage is inverted (see Figs. 5ab). If the electrical polarization is applied in the opposite direction, OVM follows the electric field and the barrier width systematically increases (going from a low resistance state to a high resistance state, see Figs. 5cd). Finally, after the maximum applied voltage is reached and the polarization is reduced, the barrier remains in a high resistance state until the voltage is reverted. Hence, OVM occurs in the opposite direction, systematically returning to a lower resistance state (Fig. 5ef). The sensitivity to oxygen mobility on the superconducting properties of underdoped GBCO is usually observed in photoexcitation experiments (attributed to changes in the oxygen order in copper chains) [36]. On the other hand, electrical polarization changing the superconducting critical temperature of YBCO / ferroelectric devices has been reported [37], which indicates that the

properties of GBCO are extremely sensitive to the electrical field. The absence of polarization hysteretic IV curves in the [G-S-G] system could be attributed to symmetric interfaces (due to smaller disorder or vacancy concentration) and to the absence of FE polarization assisting the mechanism. It is worth noting that both, the disorder at the interface and the polarization induced modification of the superconducting properties at GBCO / insulator interfaces, are significantly relevant to the design of Josephson junctions based on high temperature superconductors.

Following, we analyze the IV curves assuming that tunneling across the different barriers is the main mechanism/responsible for the electrical transport in the samples. The tunneling across an insulator barrier is usually well described by the model of Simmons [13]. The tunneling regimes depend on the bias (V), the thickness (d) and the height (ϕ) of the barrier. When a bias V >ϕ /e is applied, the tunnel transport takes place through an effective barrier thinner than its nominal thickness (called Fowler-Norheim (F-N) regime). The ϕ value may be related to the W of the electrodes and the properties of the insulator barrier. For a defect- free insulator in the Schottky limit (absence of trapped charge), the height of the barrier for the F-N regime can be estimated as the difference between the W injecting the current and the electron affinity of the insulator barrier [38]. Considering w_{GBCO}= 6.1 eV (optimal doped) [39] and w_{Nb} = 4.87 eV [40], and χ_{BTO} = 3.8-3.9 eV [41] and χ_{STO}= 3.9 eV [42], ϕ is expected to be no larger than 2.2 eV and 1 eV for the current injected across G-I_d and Nb-I_d interfaces, respectively. In the F-N regime, the tunneling current is well described by [13]

$$I = \frac{2Ae^3}{8\pi h\beta^2 t^2 \phi} V^{\alpha} exp\left(\frac{-8\pi\beta\sqrt{2m^*}\phi^{3/2}}{3he}\frac{1}{V}d\right), \text{[eq. 1]}$$

where A is the area of the barrier, β is the barrier shape correction, α = 2, d is the barrier thickness, V is the bias voltage, and e, m^* and h are the electron charge, effective mass of the electron, and the Planck constant, respectively. Considering β = 1, the equation can be rewritten as

$$\ln\frac{I}{V^2} = ln\left[\frac{2Ae^3}{8\pi h d^2 \phi}\right] + Bd, \text{[eq. 2]}$$

being B the inverse of the attenuation length of the current carriers across the insulator barrier (λ), and it is given by

$$B = \frac{1}{\lambda} = -\frac{8\pi\sqrt{2m^*}\phi^{\frac{3}{2}}}{3he}\frac{1}{V}, \text{ [eq. 3]}$$

Figures 6*ab* show the expected lineal dependence for the Log I vs. V curves for [G-S-Nb] and [G-B-Nb] (positive branches correspond to current injected from the Nb to the GBCO). The expected linear semi-log dependence is observed for the different barrier thickness. A Similar dependence was obtained for [G-S-G] and [G-B-G] (not shown). The *B* values for the different systems at positive and negative V branches were estimated from equation 2. Finally, the $\phi(m^*)^{1/3}$ values between 1 V and 2 V for the different configurations were estimated from *B* vs (1/*V*) slope according to eq. 3 (see Fig. 6*c*). Table 1 shows a summary of the obtained results considering $m^* = m_e$. For BTO barriers, ϕ values upload the voltage (↑) (from zero to $|V|$) and download the voltages (↓) (from $|V|$ to zero) were included. The ϕ ranges from ≈ 0.28eV for [G→S→Nb] to ≈ 0.5 eV for electrons injected [Nb→B→G]. Unexpectedly, for the barriers considering $W_{Nb/GBCO}$ and $\chi_{BTO/STO}$, the calculated value of ϕ is larger for electrons injected from the Nb than those injected from the GBCO. This suggests that the W value for GBCO is reduced at the interfaces by disorder. The hysteretic behavior observed for [Gd-B_d-G] and [Gd-B_d-Nb] increases the ϕ value for the higher resistive state. For example, in [G-B_d-G] heterostructures, ϕ goes from $\phi \approx 0.31$ eV (lower resistance state) to $\phi \approx 0.37$ eV (higher resistance state).

To summarize, we show that the characteristic IV curves of conducting / insulator / conducting TJs strongly depend on the properties of the electrodes and the properties of the insulator barrier. The results were analyzed assuming that tunneling across a thin insulator barrier is the main mechanism for electrical transport. For heterostructures with STO as a barrier, the tunneling current density *J* is mainly determined by the barrier thickness and the type of electrodes. No features related to OVM were observed. However, the physics involved in the heterostructures with BTO is notoriously more complex than the latter. The observed IV curves for [G-B-G] and [G-B-Nb] are in agreement with those predicted for asymmetric FETJ. This indicates that, for the former, the GBCO properties at the bottom and top interfaces are different. The presence of hysteric behavior at high polarization voltages is in

agreement with OVM affecting the barrier height (polarization systematically changes the properties of the electrodes and the barrier). This effect could be attributed to polarization inducing reversible oxygen depletion/augmentation at the interfaces, which increases the tunneling barrier height by generating insulator / conducting layers at the GBCO / BTO interfaces. Further studies would be/ required to understand the contribution of the different mechanisms to the observed electrical transport.

4. Conclusions

We have shown that the characteristics of the IV curves in conducting / insulator / conducting TJ depend on the work function of the electrodes and the properties of the insulator layer. For trilayers with STO barriers, the IV curves depend on the barrier thickness and the material used as conducting electrode. Symmetric IV curves are obtained at positive and negative branches (current injected from the top and bottom electrodes). However, asymmetric IV curves are obtained when the top GBCO electrode is changed for Nb. For trilayers with BTO barriers, hysteretic IV curves are obtained. The observed behavior corresponds to asymmetric electrodes, even for [G-B_d-B] TJs. Unlike the expected behavior for homogenous FE barriers, a clear step-like change in the resistivity for a characteristic voltage (V_c) is not observed. In addition, the hysteretic behavior does not saturate at high voltages, indicating OVM affects the barrier height. The strong sensitivity of the tunneling resistance to disorder inducing asymmetric interfaces is relevant to different applications, ranging from resistive switching memories (at room temperature) to Josephson junctions (at low temperatures).

Acknowledgments

This work was partially supported by the ANPCYT (PICT 2015-2171) and ANPCYT (PICT 2014-2237). N. H and M. S. are members of the Instituto de Nanociencia y Nanotecnología (CNEA, Argentina).

TABLE I. Summary of the energy barrier height (ϕ) for the different samples. The ϕ values for increasing (↑) and decreasing (↓) voltage ramps in the positive and negative branches are included (see Fig. 2). For the calculation of ϕ, $m^* = m_e$ was considered.

		ϕ [eV]			
	Sample	$\mathbf{V^+}\uparrow$	$\mathbf{V^+}\downarrow$	$\mathbf{\lvert V^-\rvert}\uparrow$	$\mathbf{\lvert V^-\rvert}\downarrow$
Symmetric Junction	[G-S-G]	0.33 ± 0.01	0.334 ± 0.006	0.33 ± 0.01	0.334 ± 0.006
	[G-B-G]	0.314 ± 0.006	0.362 ± 0.002	0.305 ± 0.007	0.37 ± 0.01
Asymmetric Junction	[G-S-Nb]	0.384 ± 0.015	0.381 ± 0.007	0.28 ± 0.01	0.292 ± 0.008
	[G-B-Nb]	0.492 ± 0.008	0.51 ± 0.01	0.292 ± 0.008	0.273 ±0.007

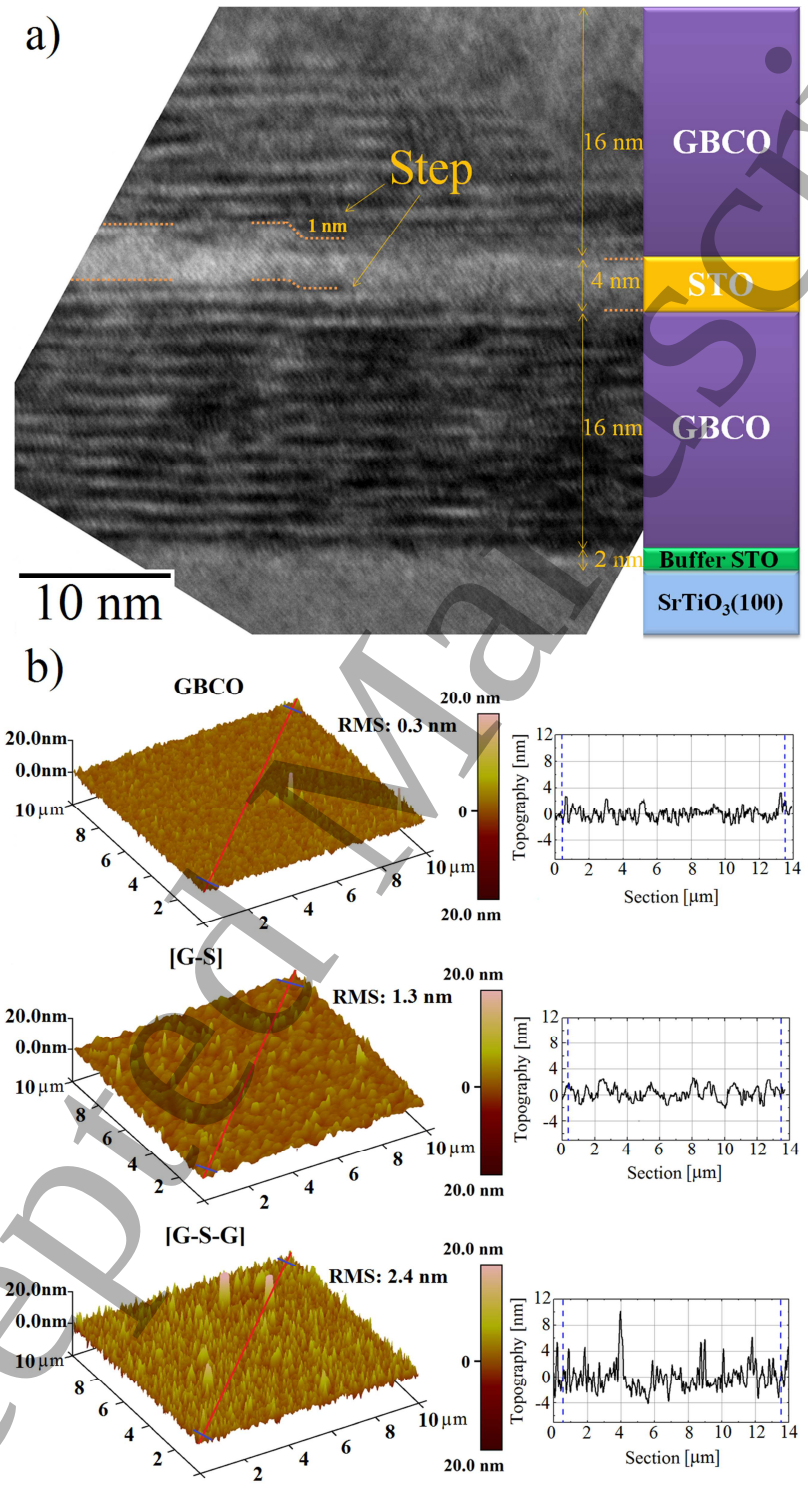

Figure 1.a) HRTEM image cross section of a [G-S_4-G] sample (left) with its corresponding schematic cross section (right). b) 10 x 10 μm^2 topographical images of: 16 nm thick GBCO thin films, [G-S_4] bilayer and a [G-S_4-G] trilayer (from top to down, respectively).

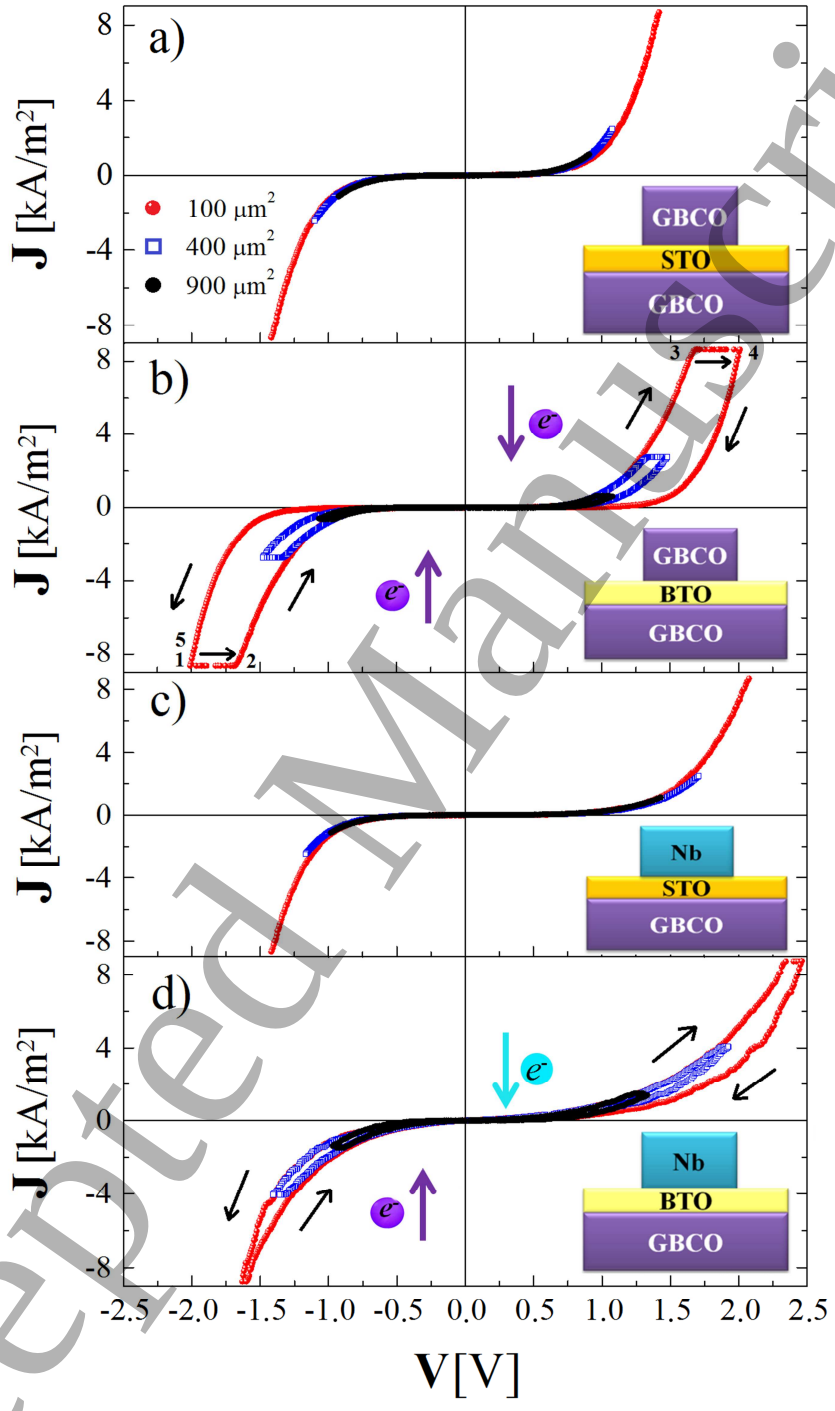

Figure 2.Typicalcurrent densities *J* as a function of the V for tunnel junctions. All the curves correspond to a barrier thickness of 4 nm. For positive voltages the current is injected from the bottom to the top electrode, and for negative voltages the current is injected from the top to the bottom electrode. For hysteretic curves, the arrows indicate if the curve corresponds to increasing or decreasing voltages. In panel b) the numbers 1 to 5 indicates the voltage way in which the IV curves are obtained. It is important to note that at both extremes of positive and negative voltage the current saturate due to the upper limit of detection.

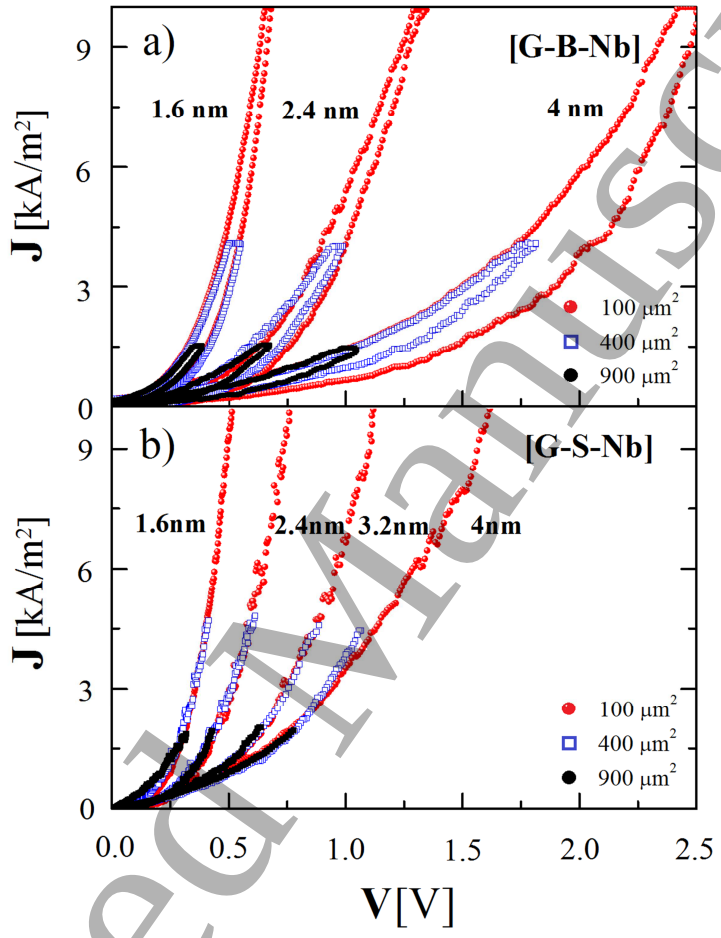

Figure 3.Current density *J* as function of the voltage (V) for the [G-S_x-G] and [G-B_x-Nb] tunnel junction of different thicknesses (with x = 1.6 nm, 2.4 nm, 3.2 nm and 4 nm) and with areas of 100 μm^2, 400 μm^2 and 900 μm^2. All the curves correspond to the positive voltage branch (current injected from the top Nb electrode).

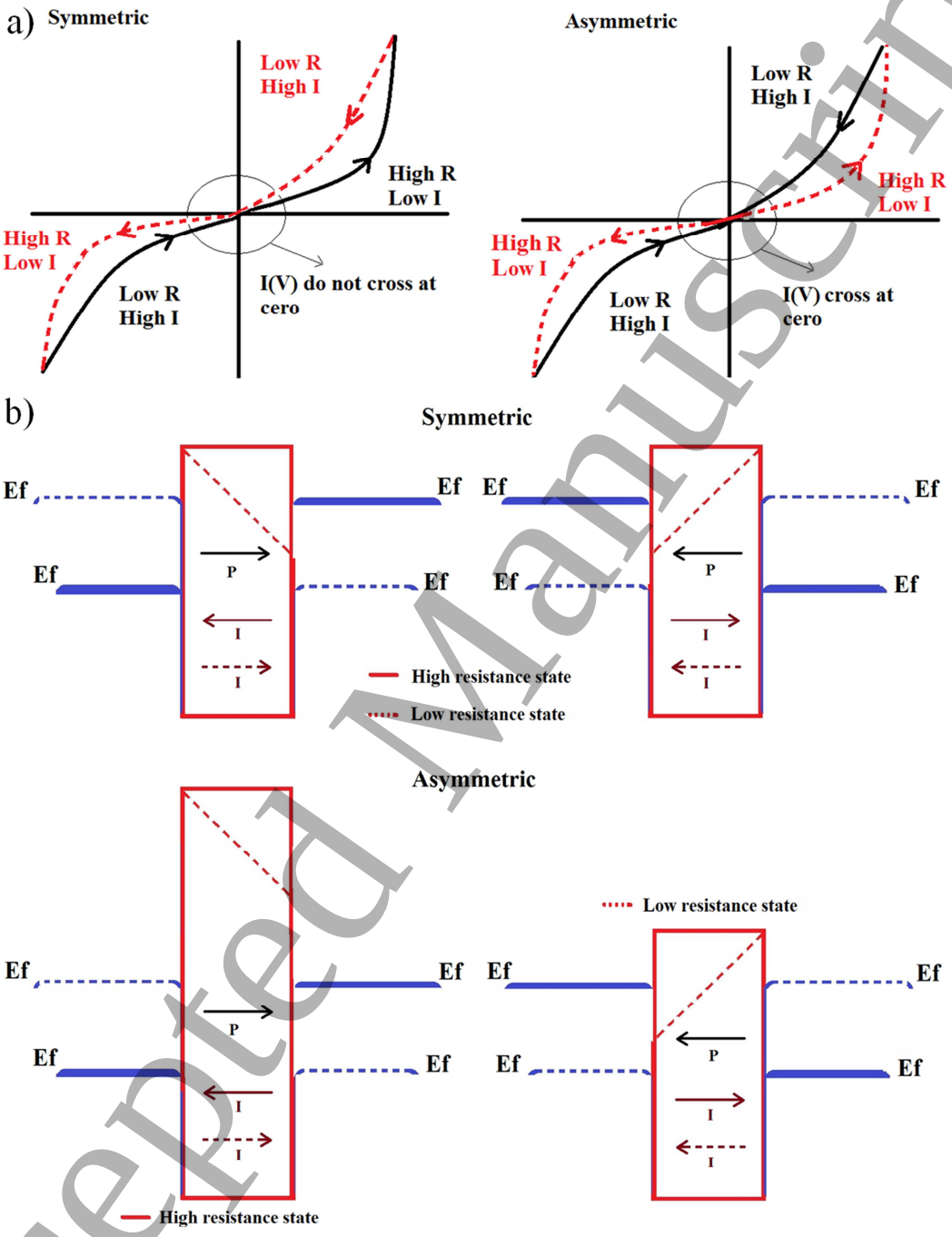

Figure 4. a) Schematic representation of the current-voltage response for symmetric ferroelectric tunnel junctions with the same electrodes (left) and asymmetric ferroelectric tunnel junctions with different electrodes (right). b) Schematic representation of the tunneling barrier energy for junctions with different ferroelectric and current orientations, parallel (solid lines) and antiparallel configurations. In the symmetric configuration the resistance state is given by the relative orientation of the current respect to the ferroelectric polarization. In the asymmetric case the change of the resistance state is triggered by the switching of the ferroelectric polarization. Ef is the Fermi energy.

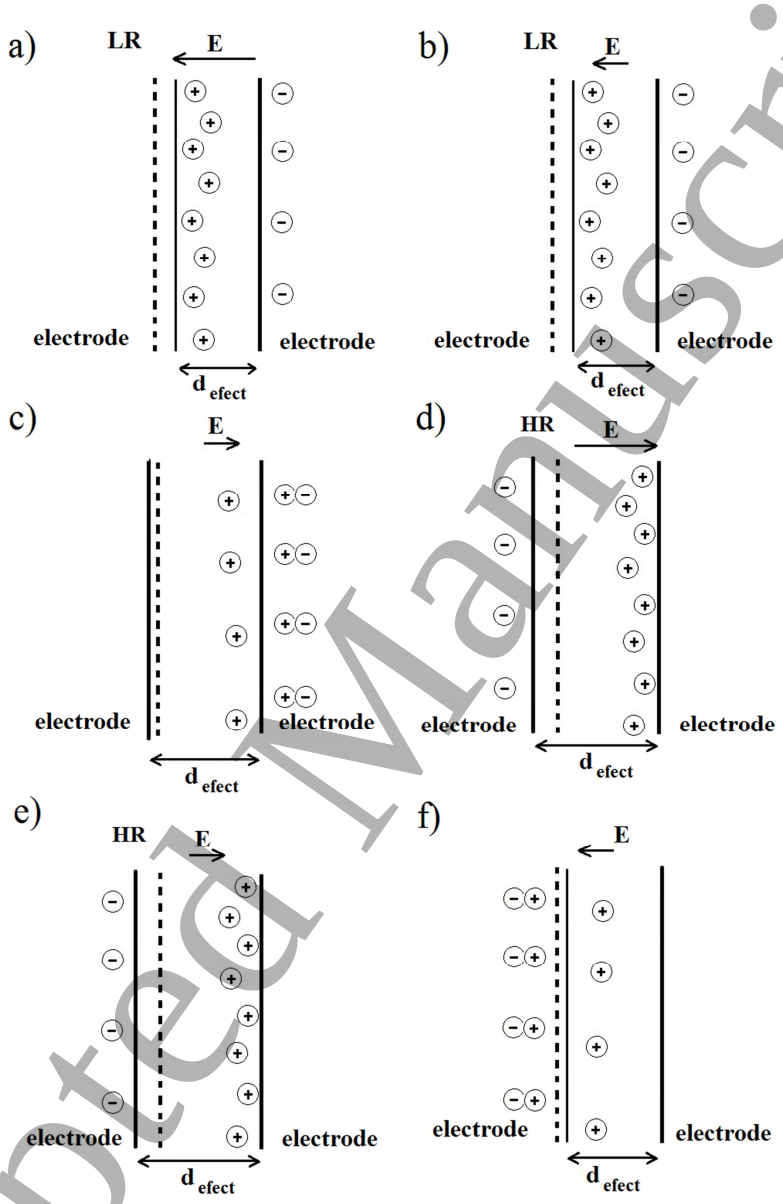

Figure 5. Schematic representation of the barrier effective thickness change considering the OVM mechanism with different applied electrical fields. Starting configuration for high negative applied field (a), decreasing negative field (b), after switching the applied field to a small positive value (c), increasing positive field (d) and finally for the decreasing positive field (e) and after the switching the applied field to a small negative value (f).

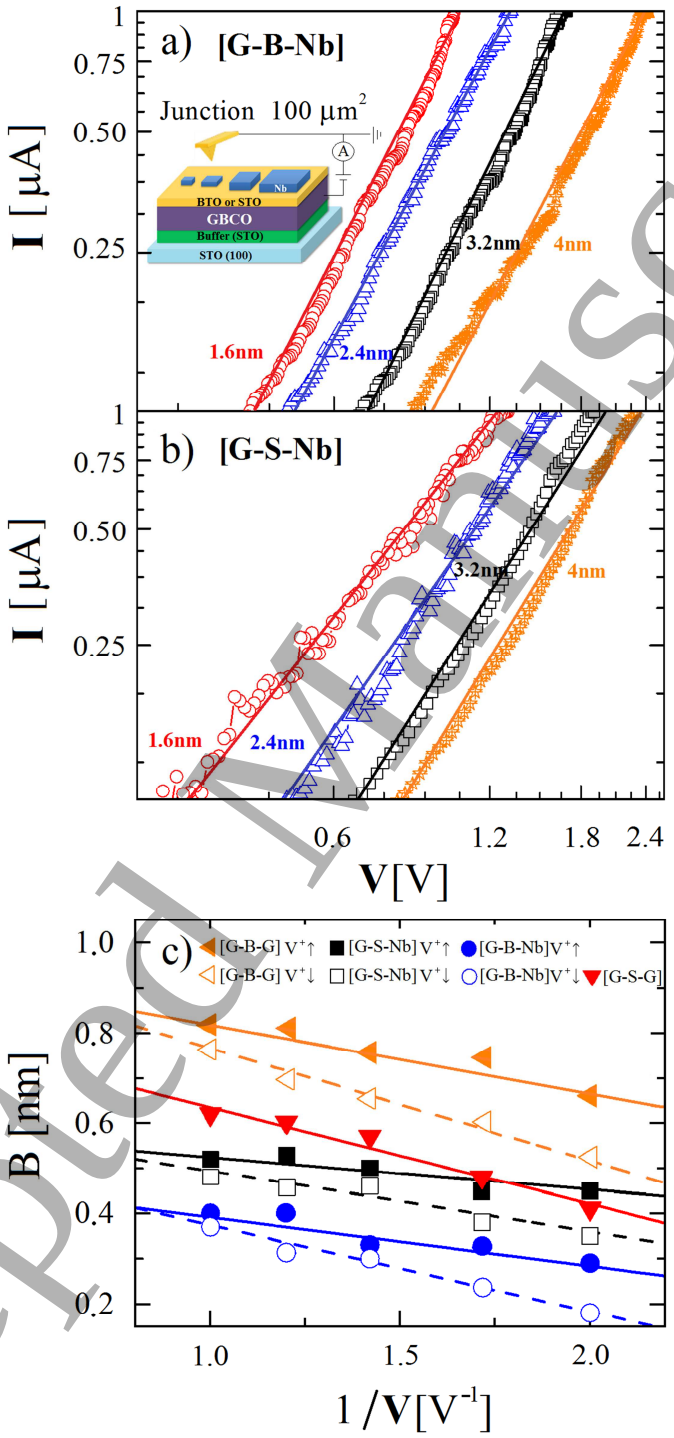

Figure 6.a-b) Current (I) vs voltage (V) curves for [G-B_d-Nb] and [G-S_d-Nb], respectively. The curves were obtained in 10x10 μm^2 junctions with x = 1.6 nm, 2.4 nm, 3 nm and 4 nm. The curves correspond to positive polarization in which the tunnel electrons are injected by the Nb electrode. Lines correspond to fits according to equation 1. c) Parameter B as function of 1/V obtained for positive voltages (electrons injected from the top electrode). For BTO barriers the curves dependence are analyzed increasing (up) and decreasing (down) voltage. Lines correspond to linear fits.

References

[1] Griffiths, D 2005 Introduction to Quantum Mechanics (Pearson Prentice Hall)
[2] Shinji Yuasa, Taro Nagahama, Akio Fukushima, Yoshishige Suzuki and Koji Ando 2004 Giant room-temperature magnetoresistance in single-crystal Fe/MgO/Fe magnetic tunnel junctions *Nat. Mat* **3** 868
[3] C. Fumeaux, W. Herrmann, F. K. Kneubühl, H. Rothuizen 1998 Nanometer thin-film Ni–NiO–Ni diodes for detection and mixing of 30 THz radiation *Infrared Phys. Technol***39** 123
[4] Giaever, I 1960 Energy gap in superconductors measured by electron tunneling *Phys. Rev. Lett*. **5** 147
[5] V. Garcia, M. Bibes 2014 Ferroelectric tunnel junctions for information storage and processing *Nat. Commun.* **5** 4289.
[6]Changjian Li et al. 2015 Ultrathin $BaTiO_3$-Based Ferroelectric Tunnel Junctions through Interface Engineering *Nano Lett.***15** (4) 2568–2573.
[7] WeimingLü et al. 2017 Multi non-volatile state resistive switching arising from ferroelectricity and oxygen vacancy migration *Adv. Mater.***29** 1606165.
[8]A. Sawa 2008 Resistive switching in transition metal oxides *Mater. Today* **11** 28
[9]Rainer Waser and Masakazu Aono 2007 Nanoionics-based resistive switching memories *Nature Mat.* **6** 836.
[10]J. S. Lee, S. Lee, T. W. Noh 2015 Resistive switching phenomena: a review of statistical physics approaches *Appl. Phys. Rev.* **2** 031303.
[11] F. A. Cuellar etal. 2014 Reversible electric-field control of magnetization at oxide interfaces *Nat. Comm.* **5** 4215.
[12] Ming Li, Jian Zhou, Xiaosai Jing, Min Zeng, Sujuan Wu, JinweiGao, Zhang Zhang, XingsenGao , Xubing Lu, J.-M. Liu, and Marin Alexe 2015 Controlling Resistance Switching Polarities of Epitaxial $BaTiO_3$ films by Mediation of Ferroelectricity and Oxygen Vacancies *Adv. Elect. Mat* **1** 1500069.
[13] J. G. Simmons 1963 Generalized Formula for the Electric Tunnel Effect between Similar Electrodes Separated by a Thin Insulating Film *J. Appl. Phys*. **34** 1793.
[14] H. Kohlstedt, N. A. Pertsev, J. Rodríguez Contreras, and R. Waser 2005 Theoretical current-voltage characteristics of ferroelectric tunnel junctions*Phys. Rev B* **72** 125341
[15] N. Reyren *et al*. 2007 Superconducting Interfaces between Insulating Oxides *Science* **317** 5842.
[16] M. Bibes *et al.* 2001 Nanoscale Multiphase Separation at $La_{2/3}Ca_{1/3}MnO_3/SrTiO_3$ Interfaces *Phys. Rev. Lett.* **87** 67210
[17] V. V. Lemanov, E. P. Smirnova, P. P. Syrnikov, and E. A. Tarakanov 1996 Phase transitions and glasslike behavior in $Sr_{1-x}Ba_xTiO_3$ *Phys. Rev. B* **54** 3151
[18] H. Béa et al 2006 Anisotropic bimodal distribution of blocking temperature with multiferroic $BiFeO_3$ epitaxial thin films *Appl. Phys. Lett* **89** 242114.
[19] K. A. Muller and H. Burkard 1979 $SrTiO_3$: An intrinsic quantum paraelectric below 4 K *Phys. Rev. B* **19** 3593.
[20] J. H. Haeni et al 2004 Room-temperature ferroelectricity in strained $SrTiO_3$*Nature* **430** 758.
[21] Na Sai, Alexie M. Kolpak, Andrew M. Rappe 2005 Ferroelectricity in ultrathin perovskite films *Phys. Rev B* **72** 020101.
[22]Junquera, P. Ghosez 2003 Critical thickness for ferroelectricity in perovskite ultrathin films *Nature* **422** 506.
[23] Y. S. Kim et al 2005 Critical thickness of ultrathin ferroelectric $BaTiO_3$ films *Appl. Phys. Lett.* **86** 102907.

[24] H. Béa et al 2006 Ferroelectricity down to at least 2 nm in Multiferroic $BiFeO_3$ Epitaxial Thin Films *Jpn. J. Appl. Phys.* **45** L187

[25] H. Navarro, Ilkyu Yan, M. Sirena, J. Kim and N. Haberkorn 2015 Characterization of the insulator barrier and the superconducting transition temperature in $GdBa_2Cu_3O_{7-\delta}/BaTiO_3$bilayers for application in tunnel junctions *J. Appl. Phys*. **118** 045308

[26] H. Navarro, M. Sirena, J. Kim, N. Haberkorn 2015 Smooth surfaces in very thin $GdBa_2Cu_3O_{7-d}$ films for application in superconducting tunnel junctions *Phys. C* **510** 21-26

[27] M. Sirena 2011 Roughness influence in the barrier quality of ferroelectric/ferromagnetic tunnel junctions, model, and experiments *J. Appl. Phys.* **110** 063923.

[28] N. Haberkorn, F. Lovey, A. Condo and J. Guimpel 2005 HRTEM study of the interfaces and stacking defects in superconducting \ magnetic perovskite superlattices *J. Appl. Phys.* **97** 53511.

[29] M. Sirena, L. Avilés Félix, N. Haberkorn 2013 High-Tc Superconductor/insulating bilayers for the development of ultra-fast electronics *Appl. Phys. Lett.* **103** 52902.

[30]D. J. Kim, H. Lu, S. Ryu, C.-W. Bark, C.-B.Eom, E. Y. Tsymbal, and A. Gruverman 2012 Ferroelectric tunnel memristor*Nano Lett.* **12** 5697

[31] N. A. Pertsev, J. Rodríguez Contreras, V. G. Kukhar, B. Hermanns, H. Kohlstedt, and R. Waserless 2003 Coercive field of ultrathin $Pb(Zr_{0.52}Ti_{0.48})O_3$ epitaxial films *Appl. Phys. Lett* **83** (16) 3356.

[32] B. Wuyts, V.V. Moshchalkov, Y. Bruynseraede 1996 Resistivity and Hall effect of metallic oxygen-deficient YBa2Cu3Ox films in the normal state *Phys. Rev. B***53** 9418.

[33] O. Cyr-Choiniere, G. Grissonnanche, S. Badoux, J. Day, D. A. Bonn,W. N. Hardy, R. Liang, N. Doiron-Leyraud, and Louis Taillefer 2015 Two types of nematicity in the phase diagram of the cuprate superconductor $YBa_2Cu_3O_y$ *Phys. Rev. B***92** 224502.

[34] N. Haberkorn, G. Bridoux, E. Osquiguil, G. Nieva, and J. Guimpel 2007 Hall effect in a$GdBa_2Cu_3O_{7-\delta}/La_{0.75}Sr_{0.25}MnO_3$perovskite bilayer, *Appl. Surf. Sci.* **254** 222.

[35] B. A. Gray et al. 2016 Superconductor to Mott insulator transition in $YBa_2Cu_3O_7/LaCaMnO_3$ heterostructures *Sci. Rep.* **6** 33184.

[36] S. Bahrs, J. Guimpel, A. R. Goñi, B. Maiorov, A. Fainstein, G. Nieva, and C. Thomsen 2005 Persistent photo-excitation in $GdBa_2Cu_3O_{6.5}$ in a simultaneous Raman and electrical-transport experiment Phys Rev B **72** 144501.

[37] Arnaud Crassous et al. 2011 Nanoscale Electrostatic Manipulation of Magnetic Flux Quanta in Ferroelectric/Superconductor $BiFeO_3/YBa_2Cu_3O_{7-\delta}$ Heterostructures *Phys. Rev. Lett* **107** 247002.

[38] I. C. Infante,F. Sánchez, V. Laukhin,A. Pérez del Pino, J. Fontcuberta, K. Bouzehouane, S. Fusil, and A. Barthélémy 2006 Functional characterization of $SrTiO_3$ tunnel barriers by conducting atomic force microscopy *Appl. Phys. Lett* **89** 172506.

[39] T. Hirano, M. Ueda, K.-i. Matsui, T. Fujii, K. Sakuta, and T. Kobayashi 1992 Dielectric Properties of $SrTiO_3$ Epitaxial Film and Their Application to Measurement of Work Function of $YBa_2Cu_3O_7$ Epitaxial Film *Jpn. J. Appl. Phys.* 31 1345.

[40]Dweydari, A. W. Mee, C. H. B 1975 Work function measurements on (100) and (110) surfaces of silver *Physica Status Solidi (a)* **27** 223.

[41] D. P. Cann, and C. A. Randall 1996 Electrode effects in positive temperature coefficient and negative temperature coefficient devices measured by complex-plane impedance analysis *J. Appl. Phys.***80** 1628.

[42] J. Robertson and C. W. Chen 1999 Schottky barrier heights of tantalum oxide, barium strontium titanate, lead titanate, and strontium bismuth tantalite *Appl. Phys. Lett.***74** 1168.